

# Experimental Study of Acoustic Ultra-High-Energy Neutrino Detection

J. Vandenbroucke,\* G. Gratta, and N. Lehtinen†  
*Physics Department, Stanford University, Stanford CA 94305*

(Dated: May 25, 2004)

An existing array of underwater, large bandwidth acoustic sensors has been used to study the detection of ultra-high-energy neutrinos in cosmic rays. Acoustic data from a subset of 7 hydrophones located at a depth of 1600 m have been acquired for a total live time of 208 days. For the first time a large sample of acoustic background events has been studied for the purpose of extracting signals from multi-EeV showers. As a test of the technique an upper limit for the flux of ultra-high-energy neutrinos is presented along with considerations relevant for the design of an acoustic array optimized for this purpose.

## INTRODUCTION

The detection of neutrinos above  $10^{19}$  eV in cosmic rays has become an important topic in particle astrophysics. It is generally assumed [1] that the flux of cosmic ray protons should drop sharply (“GZK cutoff”) between  $10^{19}$  and  $10^{20}$  eV due to pion photo-production on the microwave background. Recent measurements using the AGASA surface array [2] and the HiRes air fluorescence telescope [3] disagree on the existence of such a cutoff. Neutrinos are likely to be an important component of the particle flux at ultra-high energies. If the GZK mechanism is indeed present, the flux of ultra-high energy protons must be accompanied by ultra-high energy neutrinos from pion decay. Their clear detection would provide conclusive input to the field.

Technically, the very small fluxes available for cosmic rays at these extreme energies require unprecedented detector sizes. Therefore only detectors employing naturally occurring media are practical in this case. This constrains the techniques available for an accurate and redundant energy measurement and primary particle identification. The parallel development of several different techniques, some of which would hopefully employ the same medium, is therefore crucial to constrain the measurements and provide sufficiently accurate and redundant information for the full understanding of cosmic rays at the highest energies. Indeed, in the last few years, great progress has been made in the use of radio signals for the detection of protons and neutrinos using a variety of natural targets, including lunar regolite [4] and ice with ground- [5] and space-based [6] antennas.

In this paper we describe the first experimental results obtained with the acoustic technique in ocean water. The possibility of acoustic detection of high-energy particles was first discussed in 1957 [7]. More recently an extensive theoretical treatment of the processes relevant to the signal formation was given [8], along with its general validation at test beams on accelerators [9]. The first description of the properties of a practical, large array for ultra-high-energy neutrino detection was given in [10]. The dominant sound production mechanism, for

non-zero water expansivity, consists in the heating of the water in the region where a shower develops (instantaneously, from the point of view of acoustics), followed by an expansion producing a pressure wave. Only primaries that penetrate the atmosphere without interacting and then shower in the water are capable of producing detectable acoustic pulses, providing automatic particle identification within a broad range of energies. With respect to optical Cherenkov arrays in water (and ice) the sensors (in this case hydrophones) can be substantially more sparse because of the large ( $\approx 1$  km) attenuation length of sound in water at the frequencies ( $\approx 10$  kHz) where, for these events, most of the energy lies. As stressed in [10], the elongated shape of the showers produces acoustic interference that results in most of the sound emitted in a pancake with few degrees opening angle. This effect is important for the optimization of a detector since the optimal density of hydrophones is constrained by the ability of intercepting these relatively narrow pancakes. More generally the acoustic technique lends itself well to a calorimetric measurement of the total energy and would complement other technologies well.

## THE DETECTOR

SAUND (Study of Acoustic Ultra-high energy Neutrino Detection) is based on a very large ( $\approx 250$  km<sup>3</sup>) hydrophone array that the US Navy operates for naval exercises [11]. The array is located in the “Tongue of the Ocean”, a deep tract of sea in the Bahama islands at approximately  $24^{\circ}30'N$  and  $77^{\circ}40'W$ . A detailed description of the entire array is given in [10]. For the present work we use a subset of seven hydrophones from the large array, arranged in an hexagonal pattern as shown in Figure 1. The hydrophones are mounted on 4.5 m long booms projecting from the ocean floor. The horizontal spacing between any two hydrophones varies between 1.5 km and 1.7 km in our subset. The ocean floor is rather flat over the entire array region, with our phones located at depths between 1550 m and 1600 m. The hydrophones with their underwater preamplifiers have been

in stable operation for naval exercises since 1969.

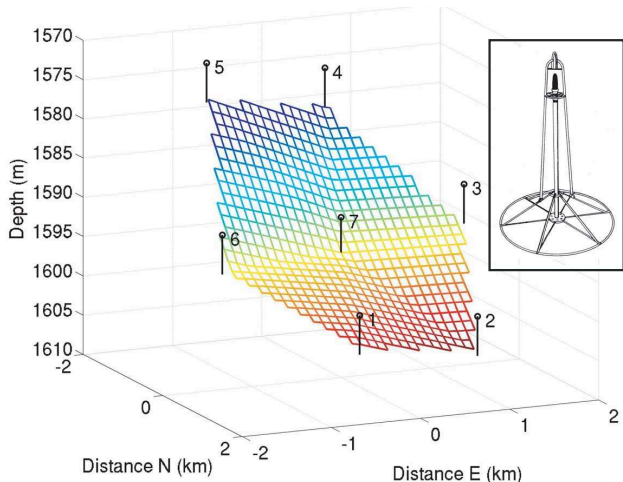


FIG. 1: Schematic view of the subset of hydrophones used for this work. The hydrophone depths are known precisely while the sea floor bathymetry between phones is obtained from a linear interpolation. The inset to the right shows details of the 4.5 m tall hydrophone deployment and support structures. The bail used to deploy the phone folds and lays on the ocean floor during operation.

After a second on-shore amplifier stage, analog signals are fed to a digitizer card [12] that continuously samples each of the seven channels at 179 ksamples/s. The time series in each channel is then fed to a digital matched filter implemented on a 1.7 MHz Pentium-4 workstation.

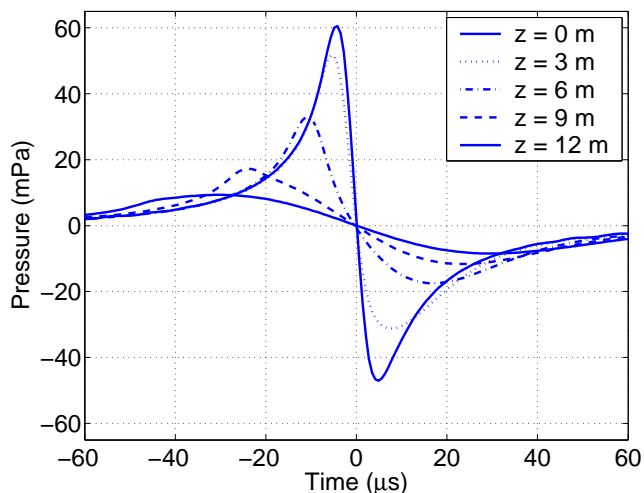


FIG. 2: Simulated acoustic signals due to a hadronic shower of energy  $10^{20}$  eV, corresponding to an initial neutrino energy of  $5 \times 10^{20}$  eV. Signals are shown at 1050 m distance perpendicular to the neutrino path. The five different curves refer to longitudinal distances of 0, 3, 6, 9, and 12 m forward from the shower maximum. [13]

Ultra-high energy neutrinos interact with matter by deep inelastic scattering on quarks inside nuclei. The interaction cross-section [14] grows with neutrino energy, increasing the chances of neutrino interaction in ocean water. After the primary interaction the neutrino energy is distributed between a quark and a lepton. The lepton on average acquires  $\sim 80\%$  of the energy [15]. The remaining energy is dumped into the water by a hadronic shower aligned with the direction of the primary neutrino. Local water heating causes an expansion and the emission of an acoustic pulse propagating in the direction perpendicular to the shower axis. Unlike in the case of  $\nu_\mu$  and  $\nu_\tau$ , for  $\nu_e$ s an electromagnetic shower is superimposed to the hadronic one. However, due to the Landau-Pomeranchuk-Migdal (LPM) effect [16], the electromagnetic shower is elongated and has an irregular structure, producing weaker acoustic signals of irregular geometry. Here we only consider the hadronic showers that exhibit the same structure for all kinds of neutrinos, and are simulated with a simple parametrization as modeled in [17]. This model includes  $\pi_0$  interactions and LPM effect for the electromagnetic components of the hadronic shower. The resulting acoustic pulse shape is then simulated, following [8, 10], at arbitrary positions  $(r, \theta)$  with respect to a hadronic shower. As shown in Figure 2 for a fixed radial distance from the shower, the bipolar pulse is tallest and narrowest in a plane perpendicular to the shower axis, at a depth corresponding to the shower maximum. The pulse becomes shorter and wider at greater longitudinal distances from the maximum. The general features of the pulse shape match the data from [9].

Triggering is achieved in SAUND with a digital filter that searches for signals matching the expected neutrino signal, appropriately weighting frequency components according to their signal-to-noise ratio [18]. The filter response function is obtained by transforming to the frequency domain the expected signal shape which is approximated by the analytical form  $S(t) \propto -(t/\tau)e^{-t^2/2\tau^2}$ . The characteristic time of the signal depends on position  $(r, \theta)$  relative to the shower (see Figure 2). A characteristic time of  $\tau = 10 \mu\text{s}$ , corresponding to the width of the largest expected signals, is chosen for the present work. The boundary of the effective volume depends somewhat on the value of  $\tau$  used, and this has been accounted for in the analysis. To obtain the filter transfer function, the expected signal in the frequency domain,  $\tilde{S}(f)$ , is divided by the noise spectrum, assumed to be of the Knudsen type [19]:  $\tilde{N}(f) \propto f^{-\alpha}$ . The expected  $\alpha = 1.7$  is approximated with  $\alpha = 2$  for analytical convenience. The transfer function  $\tilde{H} \propto \tilde{S}(f)/\tilde{N}(f)$  is then transformed to the time domain to obtain the response function,

$$H(t) = \left[ \left( \frac{t}{\tau} \right)^3 - 3 \left( \frac{t}{\tau} \right) \right] e^{-t^2/2\tau^2}. \quad (1)$$

Each channel is continuously filtered and the filter output is compared to a threshold. The filter is implemented with a discretized version of the above response function, sampled at the same frequency as the pressure waveforms (179 kHz). 12 samples ranging from  $t = -30.8 \mu\text{s}$  to  $t = 30.8 \mu\text{s}$  are used. Beyond this range the response function is below 13% of its peak amplitude. When the threshold is exceeded a trigger occurs and data are captured.

We expect the signal from the highest energy neutrinos of interest to saturate the digitizer. By simulating the effects of saturation on the digital filter we found that, for all signal amplitudes considered here, the filter triggers successfully. Indeed a class of events recorded (and rejected by some of the analysis cuts below) do exhibit signs of saturation.

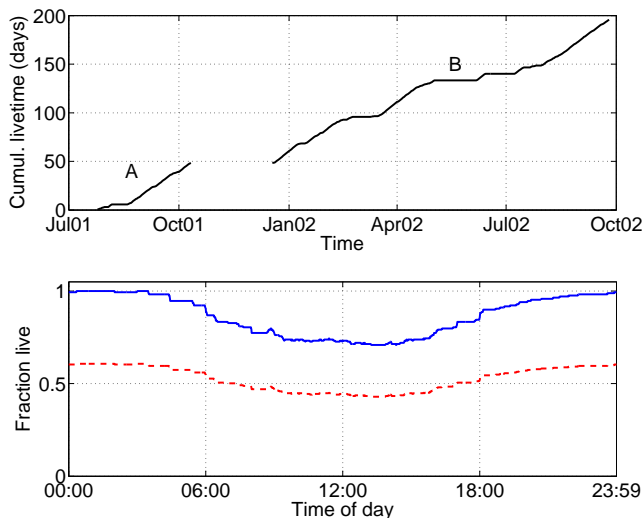


FIG. 3: Live time for SAUND. In the top panel we show the data accumulation as a function of time. A test run (Run A), not used in the present analysis, was followed by a system upgrade and a longer period of stable running (Run B). In the bottom panel the solid curve gives the live time fraction as a function of the time of the day, for days when SAUND data was collected in Run B. The dashed curve represents the data used for the analysis reported here, and it excludes several days affected bad weather or hardware failures.

By arrangement with the US Navy, the SAUND data acquisition system (DAQ) is connected to the hydrophone array only when the array is not in use for Navy exercises. The live time achieved under this agreement is shown in Figure 3. As shown in the top panel a test run (Run A) was used to commission the system and is not used for the present analysis. The system was upgraded from Oct 2001 to Dec 2001 and run for an integrated 146 days live with stable conditions (Run B). Only this stable run is used for the analysis presented here. The solid curve in the bottom panel shows what live time is achieved at different times of the day. The live time

is close to 100% at night, when no Navy tests are conducted, and it drops to about 70% in the middle of the day. The average over a day is  $\sim 86\%$ . In addition an overall live time reduction is due to weather conditions and hardware failures, resulting in the dashed line in the bottom panel of Figure 3.

Since the noise environment is volatile, an adaptive trigger threshold is used. Every minute the threshold is raised or lowered based on whether the number of events in the previous minute was above or below the target rate of 60 events/minute. Events are accumulated in memory each minute and written to disk along with header information. The distribution of thresholds in Run B is shown in Figure 4. To simplify on-line processing and off-line event reconstruction, the value of the threshold used can only change in discrete steps (the step size is 0.004 in the units appropriate for the output of the digital filter). For the purpose of neutrino analysis, only thresholds between 0.012 and 0.024 are used. These “quiet” periods account for 37% of Run B.

In total Run B contains  $\sim 20$  M triggers ( $\sim 250$  GB) corresponding to  $\sim 1.7$  GB/day. Every few weeks, data are transferred to an external hard drive that is shipped to Stanford for offline analysis. Nine-tenths of the triggers are captured for 1 ms; one-tenth are captured for 10 ms in order to study reflections from the ocean bottom.

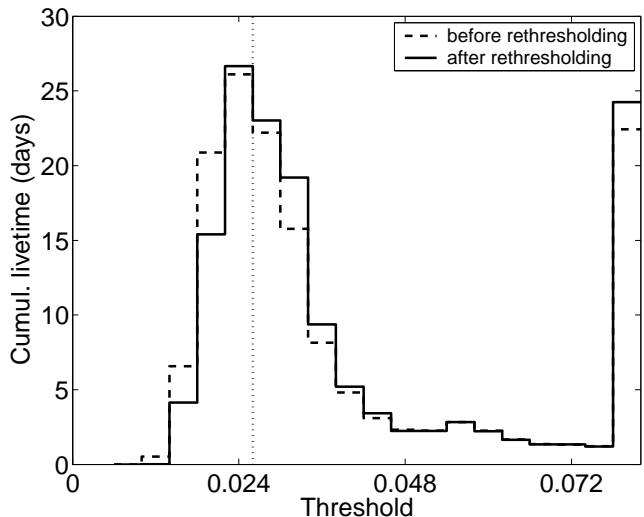


FIG. 4: Integrated livetime at each discrete threshold. The distribution has a long tail extending beyond the range shown here; this tail has been added to the last bin of the figure. The threshold step size is 0.004. The four values from 0.012 to 0.024 (left of the vertical line) are considered “quiet” and used for the present analysis. The dashed histogram represents the same quantity, after the offline re-thresholding described in the text.

The frequency response of the hydrophone/amplifiers chain is flat to better than 8 dB between 8 kHz and

50 kHz. A sharp cutoff of 100 dB/octave below 8 kHz is due to an analog high pass filter in the system, while a somewhat slower roll-off, due to the sensor itself, occurs above 50 kHz. The low frequency cutoff, while not ideal for neutrino detection, is not a significant hindrance.

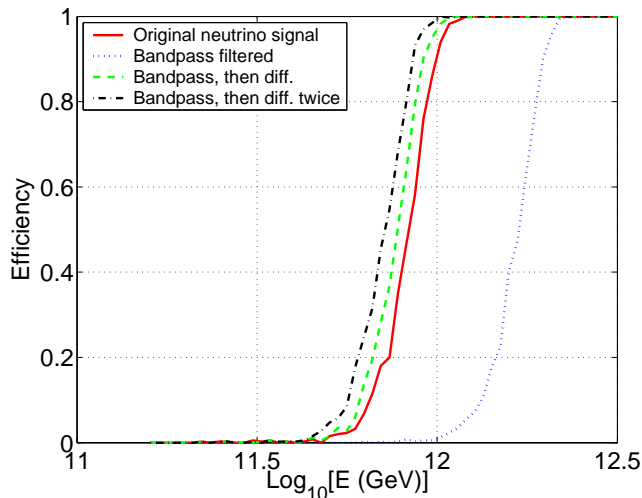


FIG. 5: Neutrino trigger efficiency for various assumptions about the AUTECH hardware transfer function, as described in the text. Curves are averaged over the “quiet” threshold distribution in Figure 4. The curves span a factor of 2 in energy threshold, and the worst case (highest threshold) is assumed to compute the efficiency of the present analysis.

The impulsive response of the hydrophone/amplifiers chain is difficult to measure and at present is not well known. In order to gain some quantitative understanding of the possible effects of it on the trigger, the efficiency of the filter was calculated for the pulse shapes in Figure 2 and for their first and second time derivatives, after applying a 9th-order Butterworth bandpass filter to mimic the AUTECH frequency response. The trigger efficiency for neutrino detection for each of these hardware transfer functions is given in Figure 5. The worst case (highest threshold) is used for the analysis presented here.

In addition to the matched filter described above, one further, *ad hoc*, selection criterion is applied at trigger level to remove a specific kind of noise that is time-correlated in all channels. This noise consists of simultaneous sinusoids in all 7 channels, occurring in bursts with 60 Hz repetition rate. While the origin of these signals is unknown, it is clear that they originate from electrical pickup, since the sound velocity does not allow for simultaneous events in all phones. The trigger removes this noise by rejecting events with large 7-channel pairwise correlation,

$$C = \sum_{i < j} \sum_t p_i(t)p_j(t), \quad (2)$$

where the time sum is taken over discrete samples and  $p_i$  is the pressure time series at phone  $i$ , normalized by

mean absolute amplitude:  $p_i = P_i / \langle |P_i| \rangle$  where  $P_i$  is the absolute pressure. Events with  $C > 500$  are removed.

Every 10 minutes time series for all channels are collected for 100 ms in forced mode. These data are used for offline noise analysis and for simulating the noise conditions in our efficiency calculation. In addition, every minute a Fourier transform is calculated from a 100 ms-long time series as shown, for a representative case, in Figure 6.

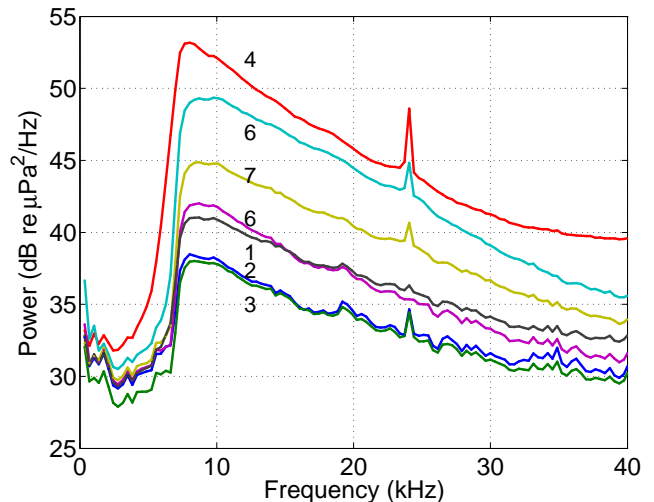


FIG. 6: A typical average noise spectrum as measured by SAUND in Run B. The plot shows the spectrum averaged over 10 hours from midnight to 10:00 AM on Dec. 22, 2001. The range of noise levels is mainly due to variations in amplifier gains. Note the 7.5 kHz high-pass filter and the  $\sim 24$  kHz peak from a transmitter used by the Navy.

SAUND Run B provides the largest data set ever collected for the purpose of studying the suitability of acoustic techniques in UHE particle detection. During the run it has been our strategy to collect data with consistent and stable conditions for an extended amount of time. A number of improvements in terms of trigger efficiency, stability and uniformity across different circumstances have been gradually developed using the data from Run B, but will only be implemented in the future.

## ENERGY AND POSITION CALIBRATION

A first understanding of the performance of the array for detecting impulsive signals can be obtained by producing small underwater implosion. This can be conveniently achieved by sinking in the detector region light bulbs that spontaneously break at some depth releasing energies of order or 100 J[20]. A calibration run of this type was performed on the morning of July 30, 2001 (technically in Run A). The small boat used for the operation was positioned over the central hydrophone using a

handheld Global Positioning System (GPS) receiver [21]. The boat engine was then turned off and several light bulbs where sunk as the vessel drifted for about half hour. Two more GPS fixes where acquired during the calibration.

The waveforms recorded for one of the implosion events are shown in Figure 7. The first pulse corresponds to the direct acoustic signal arriving to the central hydrophone. The pulse around 0.2 s corresponds to the arrival to the hydrophone of the signal reflected by the surface of the ocean. Direct pulses in all other six hydrophones appear between 0.4 s and 0.5 s, followed, in turn, by the respective surface reflections. In Figure 8 the waveform for the central hydrophone is shown on an expanded time scale, clearly showing the bottom reflection around 6 ms. Also shown in the figure is the structure of the direct pulse. The signal is expected to be a damped sinusoid, generated by the “breathing” oscillations of the gas bubble produced by the bulb. In our case the primary resonant frequency of the bubble at a depth of 100-200 m depth, is calculated to be 700-1300 Hz [22]. The signal shown in Figure 8 shows a second peak at about 1 ms, consistent with the predicted waveform sampled after a 7.5 kHz high-pass filter.

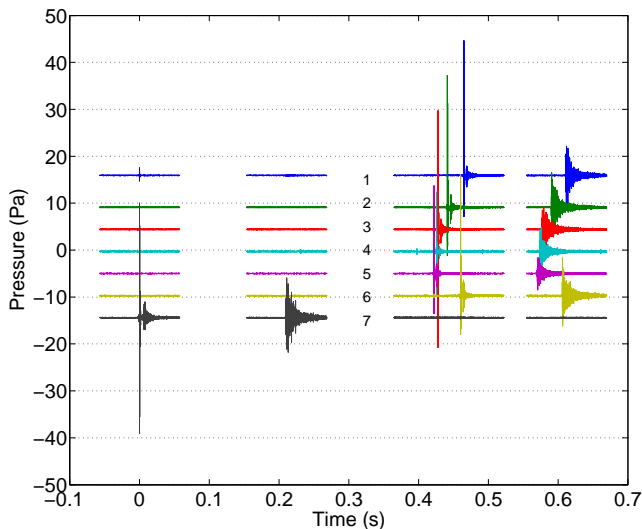


FIG. 7: Signals from a light bulb (Bulb 1) implosion. Time series from all seven hydrophones are shown. A direct signal on the central hydrophone is immediately followed by a bottom reflection and, much later, by signals from the reflection off the ocean surface. Similar sets of 3 signals appear, at a later time, on the surrounding six hydrophones. The signals in different channels are displaced vertically for clarity. The small glitch near the origin of time for phone 1 is due to electrical cross-talk.

A time-difference of arrival (TDOA) [23] analysis can be used to reconstruct the 3D location of acoustic events. This method uses only timing information. In an isotropic medium, the difference in arrival times between

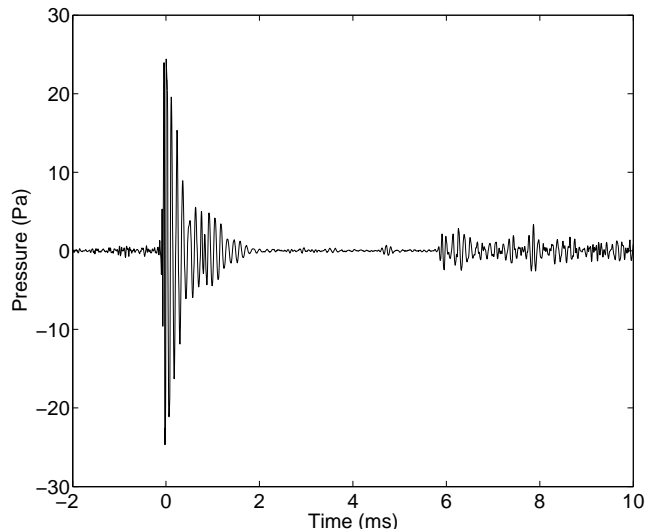


FIG. 8: Detail of the signal from Bulb 1 at the central hydrophone. Both the direct signal and, after a 6 ms delay, the bottom reflection, are evident. The oscillations in the envelope of the direct signal are due to a combination of the bubble rebound from the implosion [22] and the impulsive transfer function of the hydrophone, cable and amplifiers.

each pair of hydrophones constrains the source location to a hyperboloid. Four hydrophones (three independent time differences) are necessary to determine three hyperboloids, the intersection of which can be found analytically [24] and generally results in two points. For a planar array near the bottom, such as ours, one of the two solutions is usually reconstructed below the sea floor and it is easy to discard.

The ocean, however, is not isotropic but is a layered medium, with the value of the sound velocity (SVP) depending on the depth as shown in Figure 9. Hence sound rays are refracted as illustrated in the same Figure. Over the scale of the hydrophone distances and depths in our setup ( $\sim 1$  km) refraction significantly affects the position reconstruction. The effect can be geometrically interpreted as a warping of the TDOA hyperboloids and as a result an analytical solution is no longer possible. A numerical solution is sought by minimizing the metric

$$m(\vec{s}) = \frac{1}{N-1} \sum_{i < j} [t_{ij}^{meas} - t_{ij}(\vec{s})]^2 \quad (3)$$

with respect to  $\vec{s}$ , the test location for the acoustic source. Here  $t_{ij}^{meas}$  is the measured TDOA between phones  $i$  and  $j$  ( $t_{ij}^{meas} = t_i^{meas} - t_j^{meas}$ ) and  $t_{ij}(\vec{s})$  is the theoretical difference in arrival times for a source at  $\vec{s}$  ( $t_{ij}(\vec{s}) = t_i(\vec{s}) - t_j(\vec{s})$ ). For  $N$  phones recording a signal, the sum occurs over the  $N-1$  independent pairs of arrival times.

The theoretical travel time from the test source location to phone  $i$ ,  $t_i(\vec{s})$ , is calculated using a ray trace algo-

algorithm that divides the water into layers in each of which the sound speed is a linear function of depth. The ray follows the arc of a circle within each layer [25]. Practically, the ray trace is too time intensive to be performed for each test source location. For each phone, a table of travel times from points on a grid spanning the detector volume to the phone is built. The minimization begins at the best grid point, and the grid is linearly interpolated to find the off-grid source location. The grid is built once, and the interpolation then occurs for each event reconstruction. While the local SVP is measured almost daily by the Navy and it is available to us, it is found that seasonal SVP variations introduce errors smaller than those due to the uncertainty in the hydrophone location. Hence a single table built from an average SVP is used for all reconstructions. The position reconstruction algorithm takes a few seconds to run on a 1.6 GHz Athlon CPU (offline computer).

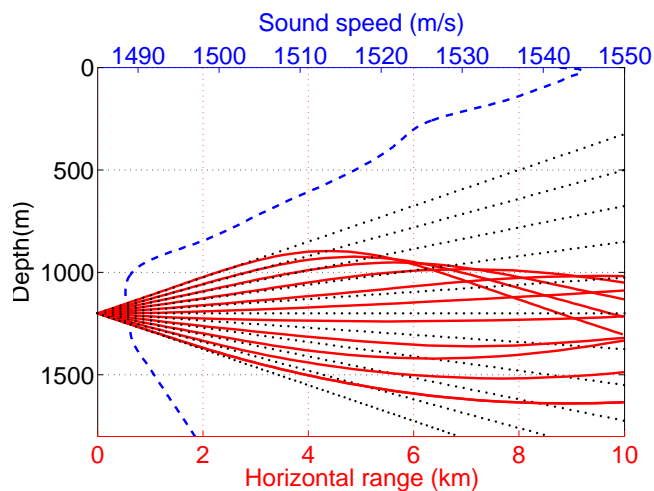


FIG. 9: Example of ray trace showing the effects of refraction. 11 rays are emitted from a source at 1200 m depth, from  $5^\circ$  below to  $5^\circ$  above the horizontal. Refracted (solid) and unrefracted (dotted) rays are plotted together for comparison. For reference, the sound speed as a function of depth (“sound velocity profile”), used to calculate the ray trace, is also shown (dashed).

Because the amplitude of light bulb implosions was far above noise, their TDOA localization was performed using all 7 direct signals (6 independent time differences), rather than 5 as used for triggered events in neutrino mode. The reconstructed depth of implosion,  $D$ , was then used to estimate the energy released in the implosion,  $P_{\text{amb}}V$ , where  $P_{\text{amb}} = \rho g D$  is the ambient pressure at the reconstructed implosion depth,  $\rho$  is the approximate density of sea water ( $\rho = 1 \text{ g/cm}^3$ ),  $g$  is the acceleration of gravity and  $V \sim 150 \text{ cm}^3$  is the volume of the light bulb. The ambient pressure at implosion (bulb failure pressure) is found to be of order 1000 kPa, while the

internal pressure of the bulbs is believed to be slightly below one atmosphere (70-90 kPa [22]). The total acoustic energy can be reconstructed independently from a phone  $i$  as:

$$E_{\text{det}}(i) = \frac{4\pi r^2}{\rho c} \int P^2(i, t) dt, \quad (4)$$

where  $P(i, t)$  is the recorded pressure time series at phone  $i$ , and  $r$  is the distance from implosion to phone. Lensing effects due to the changing sound velocity as a function of depth were studied and found to be negligible for the geometry discussed here.

The horizontal reconstructed positions of the light bulb implosions are shown in Figure 10, along with the three GPS fixes of the boat from which they were dropped. The implosions are sequentially numbered in the order they occurred. The GPS points, shown with the  $\pm 15 \text{ m}$  errors quoted by the specifications of the instrument, are in good agreement with the TDOA reconstruction. The extent of the drift is consistent with a current of about  $5 \text{ cm/s}$  (0.1 knot).

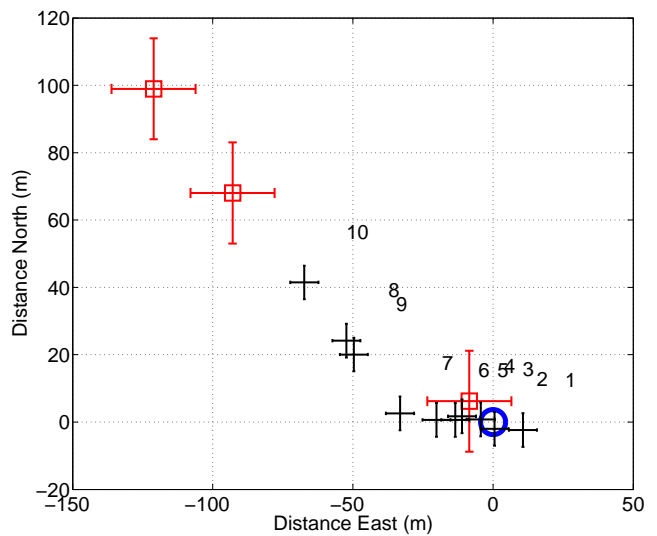


FIG. 10: The trail of implosions of bulbs dropped from a drifting boat, as reconstructed from time-differences of arrival. The reconstructed positions are indicated by crosses, with bulb labels offset for clarity. The boat’s motor was cut after starting approximately above the central hydrophone (marked by a circle). The larger crosses represent the boat positions measured at three times with a GPS device [21]. Bulbs are numbered by the order in which they were dropped. The bulb drop spanned one half hour. The lag between boat and bulb positions is consistent with a relative current between the sea surface and implosion depth of order  $1 \text{ m/s}$ .

The results of depth and energy reconstruction for the implosions are shown in Table I. The uncertainty of position reconstruction near the surface directly above the center of the array (the optimal location for source local-

TABLE I: Parameters of the implosion calibration events.  $D$  is the reconstructed implosion depth and  $P_{\text{amb}} = \rho g D$  is the ambient pressure at such depth. Here  $\rho \simeq 1\text{g/cm}^3$  is the density of sea water and  $P_{\text{amb}}V$  is the implosion energy, with  $V = 150\text{ cm}^3$  the bulb volume.  $E_{\text{theor}}$  is the theoretical detectable acoustic energy, assuming 4% conversion of the energy  $P_{\text{amb}}V$ , as appropriate for implosions triggered with a hammer device [22].  $E_{\text{theor}}$  includes the effects of absorption and the SAUND’s frequency response. The somewhat lower yield observed ( $E_{\text{det}}$ ) is consistent with the expectation of lower acoustic coupling for implosions at failure pressure [22].

Bulb	$D$ (m)	$P_{\text{amb}}$ (kPa)	$P_{\text{amb}}V$ (J)	$E_{\text{theor}}$ (J)	$E_{\text{det}}$ (J)
1	170	1640	250	3.1	1.7
2	110	1120	170	1.9	0.3
3	150	1430	210	2.6	1.5
4	170	1690	250	3.2	2.8
5	130	1300	200	2.3	0.8
6	110	1050	160	1.8	0.4
7	90	900	140	1.5	0.1
8	140	1380	210	2.5	1.9
9	200	1930	290	3.8	1.9
10	300	2930	440	6.7	1.8

ization) is 5 m. The implosion pressures  $P_{\text{amb}}$  are consistent with the literature [22]. The efficiency of conversion from  $P_{\text{amb}}V$  to acoustic energy is found to be somewhat less than the few percent quoted in [22], as expected because the bulbs are allowed to implode at failure pressure rather than being artificially ruptured at lower ambient pressure. There is large variation in the signal energies, which may also be due to implosion occurring at failure pressure. The acoustic frequency spectrum from the implosion is known to be peaked around the air bubble resonant frequency of  $\sim 1\text{ kHz}$ , well below AUTECS’s low frequency cutoff. Roughly one-half of the acoustic energy lies within AUTECS’s bandwidth. The measured spectrum and a theoretical spectrum due to the implosion event assuming 4% conversion efficiency and a source modeled by a breathing air bubble [26] agree well in the 7.5-55 kHz range.

## DATA REDUCTION

The online trigger system is designed to select impulsive bipolar signals, while rejecting most of the Gaussian noise. Because of the novelty of the technique, trigger conditions are chosen to be rather loose and substantial background is left to be rejected by off-line analysis. Impulsive backgrounds to UHE showers are expected to arise from a variety of artificial and natural sources. In particular a number of animals, from large cetaceans to small crustaceans, are known to produce high fre-

TABLE II: Event rates and neutrino efficiency at different stages of trigger and data reduction. Note that cuts 1-3 are applied to single-phone events, while the cuts in 4 are applied to coincidences between 5 phones. The “Events” column gives the number of events surviving a particular cut.

Cut	Description	Events
1)	Online Triggers	
	a) digital filter	64.6 M
	b) correlated noise	20.2 M
2)	Quality Cuts	
	a) offline re-thresholding	7.23 M
	b) offline quiet conditions	2.60 M
	c) $\Delta t_0 > 1\text{ ms}$	2.56 M
3)	Waveform Analysis	
	a) remove spikes	2.03 M
	b) remove diamonds	1.96 M
	c) $f_e > 25\text{ kHz}$	1.92 M
4)	Coincidence Building	
	a) coincidence windowing/hit phone geometry	948
	b) convergence	79

quency acoustic transient noises. While the Tongue of the Ocean is relatively isolated from the open ocean and hence rather quiet, an important motivation for this first large-volume data-taking campaign is indeed the exploration of such “coherent” backgrounds. Offline data reduction is used to select events consistent with neutrino-induced showers while rejecting backgrounds in SAUND Run B. The efficiency of each step of data reduction is estimated using simulated neutrino events to which, as discussed above, bandpass filtering is applied to account for the known frequency response of the array. As is also described above, the unknown phase response of SAUND is addressed by repeating the efficiency analysis with the first and second derivative of the simulated and filtered signal. The worst case (lowest efficiency) is assumed in the subsequent analysis.

The first step in offline data analysis is a set of data quality cuts. These are particularly important because of the volatility of the background noise. The adaptive thresholding algorithm used online was in some case found to be too slow in reacting to the changing conditions. Offline re-thresholding is hence applied to stabilize the rate to 60 events/minute. After offline re-thresholding the cut selecting “quiet” events is repeated. Finally, events with  $\Delta t_0 < 1\text{ ms}$  are removed, where  $\Delta t_0$  is the difference in time stamps between the current event and the previous one. This last cut rejects bursts of events that occasionally occur in the data set. The combination of event quality cuts reduced the sample from Run B from 20.2 million to 2.56 million events, with an estimated neutrino efficiency of  $> 99\%$ .

Waveform analysis is then used to further reduce the

background. A powerful method of event classification is provided by the scatter plot between effective frequency  $f_e$  and duration in effective number of cycles  $n_e$ . We define the effective frequency as

$$f_e = \frac{1}{2\pi\Delta t} \cos^{-1} \left[ \frac{\langle P(t)P(t+\Delta t) \rangle}{\langle P^2(t) \rangle} \right], \quad (5)$$

where  $P(t)$  is the recorded pressure time series and  $\Delta t$  is the sampling time ( $5.6 \mu\text{s}$ ), small compared to the signal oscillation period. The effective duration in number of cycles is given by  $n_e = D_e f_e$ , where

$$D_e = \frac{E_S}{\frac{1}{2}P_{\text{peak}}^2} \quad (6)$$

is the duration of the signal in units of time. Here  $P_{\text{peak}}$  is the maximum absolute amplitude of the recorded time series and

$$E_S = E_{S+N} - E_N = \int P^2(t)dt - \int P_{\text{rms}}^2 dt, \quad (7)$$

where  $P_{\text{rms}}$  is determined from the noise spectrum calculated once per minute. The normalization is such that a sinusoid, in the limit of many periods in the capture window, will give  $n_e$  equal to the number of cycles of the sinusoid. The scatter plot between these two parameters is shown in Figure 11 for the 2.56M events left in the data set. Also shown in Figure 11 is the envelope between the regions containing 95% of the neutrinos simulated, filtered and differentiated as described above.

The general region marked “s” in the scatter plot includes events, here called “spikes,” in which a single digital sample is displaced from the rest of the waveform. Spike events occur in bursts with a 50 Hz rate and ceased when a large radar system near out DAQ system was disabled. We reject spike events with a specific filter using the metric

$$m_{\text{spike}} = \frac{M_1(|P|) - M_2(|P|)}{M_2(|P|)} \quad (8)$$

where  $P$  is the pressure time series and  $M_1$  and  $M_2$  give the largest and second-largest amplitude samples, respectively. Events with  $m_{\text{spike}} < 0.7$  are retained. The region of Figure 11 marked “d” includes events, here called “diamonds,” consisting of a diamond-shaped envelope containing many cycles. These events, an example of which is shown in the top panel of Figure 12, are believed to be genuine acoustic signals produced by marine mammals swimming in the area. They can be rejected with a digital matched filter whose response function was constructed by averaging 10 hand-picked examples of good diamond events. The diamond rejection metric,  $m_{\text{diamond}}$ , is defined for a given waveform to be the maximum output of this digital filter acting on the waveform. Events with  $m_{\text{diamond}} < 0.7$  are retained.

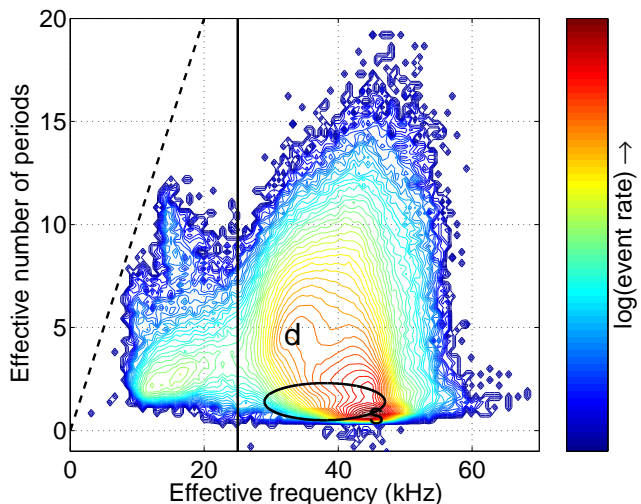


FIG. 11: Scatter plot between effective frequency and number of periods as defined in the text. The dashed line represents an upper bound due to the length of the capture window (1 ms). The events clustered near this line are due to Navy pingers at specific frequencies. The solid vertical line indicates a cut discussed in the text. The ellipse indicates the envelope approximate locations of the simulated neutrino events with different combinations of filtering and differentiation as discussed in the text. The letters “s” and “d” identify regions where “spike” and “diamond” -type events cluster.

Finally, neutrino candidates are required to have  $f_e > 25$  kHz. This cut eliminates low frequency noise originating from natural (e.g. whale calls) as well as artificial sources (e.g. boats, AUTEK pingers).

The waveform analysis reduces the data set from 2.56M to 1.92M events, retaining  $\sim 93\%$  of the simulated neutrino events.

Coincidences between different hydrophones are then reconstructed in the reduced data set. In a first step the reconstruction program finds cases in which 5 different phones have events in a 2.267 s coincidence window. This window is the maximum possible time delay between phones plus a 10% “buffer” to account for measurement errors and refraction. We then require that each pair of events in the 5-event coincidence satisfies causality (with a 10% buffer). Finally we apply a phone geometry cut: There are 21 ways to choose 5 of the 7 phones. 6 of these combinations, those forming a trapezoid, are consistent with a pancake radiation pattern triggering all phones enclosed by the pattern. Only coincidences triggering one of these 6 phone combinations are retained. These timing and geometrical cuts greatly reduce the data set, from 1.92M to 948, retaining an efficiency of 95% for neutrino events. Such a substantial data reduction is essential in order to perform the computationally intensive origin localization with TDOA in a layered medium. A given single-phone trigger may be

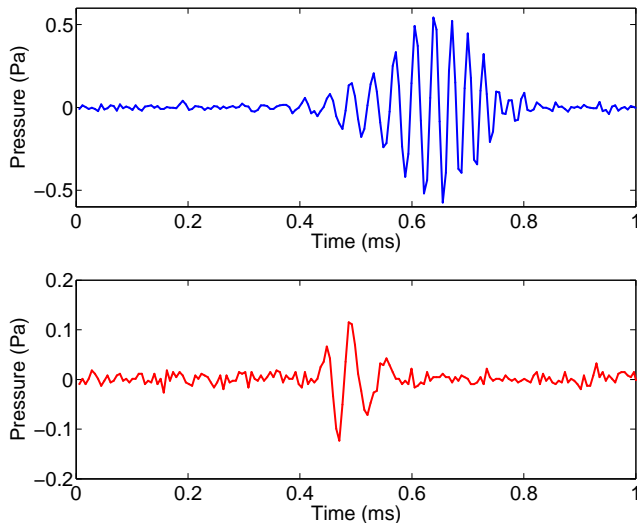


FIG. 12: Waveforms of background events. Upper panel: diamond events (see text). They are easily rejected by a dedicated digital matched filter. Lower panel: The second class of background events, “multipolars”. Depending on the phase response of the SAUND detector, these events could be indistinguishable from neutrino signals.

included in several (even many) 5-trigger coincidences. While only four phones are required for TDOA localization, 5-phone coincidences further constrains the reconstruction, reducing the background without significantly decreasing the neutrino efficiency.

For most coincidences TDOA does not converge on a consistent solution to the causality equations (solved numerically, accounting for refraction with ray-trace tables). These coincidences are presumably accidental and are therefore discarded. Most of the 79 events left in our data set have more than one of the time series of the general type shown in the bottom panel of Figure 12, here named “multipolar” events. It is apparent that this class of events may be difficult to separate from genuine neutrino signals on the sole basis of pulse-shape properties. To explore the properties of multipolar events we have built a digital matched filter using the average of 11 waveforms from events manually chosen as good examples of this event type. By applying the matched filter to earlier stages of the event selection it was also found that multipolar events tend to accumulate in periods of large adaptive threshold, and many such events in the original data set are rejected by the “quiet conditions” (2b) cut. Clearly a full pulse-shape calibration, including phase, of the acoustic sensors and their readout chain will be essential for future detector arrays. For the present data set we conservatively do *not* use the multipolar event digital filter. As will be shown in the next section, geometrical considerations make the great majority of these events inconsistent with a neutrino origin.

## ACCEPTANCE ESTIMATE

The Monte Carlo (MC) simulation used to estimate the detector efficiency is run for a set of discrete primary neutrino energies. For each energy, detection contours, examples of which are given in Figure 13, are calculated by determining the pressure pulse at each point in space (accounting for attenuation) and then applying the digital filter. For each energy  $N_{MC} = 10^5$  simulated neutrino events are produced with random orientations and positions in a water cylinder of radius 5 km, centered around the central phone. The detection contour is then “bent” to account for refraction and its intersection with the different phones in the array is tested as shown, for a particular configuration, in Figure 14. For an energy  $E$  and required minimum number of phones hit  $N_{min}$ , the acceptance is then given by  $A(E, N_{min}) = A_0 N / N_{MC}$ , where  $N$  is the number of Monte Carlo events with at least  $N_{min}$  phones hit and  $V_0$  and  $\Omega_0$  are, respectively, the volume and the solid angle over which Monte Carlo points are chosen.

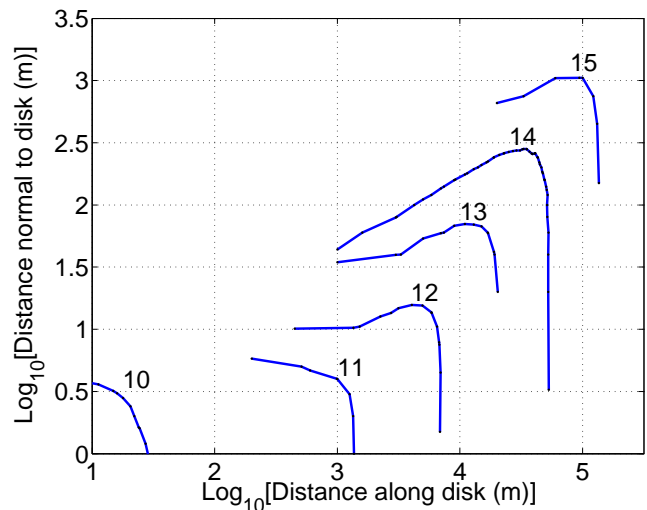


FIG. 13: Neutrino detection contours for SAUND, for a trigger threshold of 0.02. In the plot the neutrino producing the shower is propagating along the vertical axis. The shower maximum is at the origin of the coordinate system. Curves are labeled by  $\log_{10}[E(\text{GeV})]$ . Only one quadrant is represented.

In order to optimize the algorithm a first scan is performed on the entire volume using a coarse grid. From this scan it was found that, for our geometry, events in the top 1100 m have no chance of producing a five phone coincidence. Hence events for the scan on a finer grid were only produced in the bottom 500 m of water. Although the outer hydrophones are only 1.5 km from the central one, it was found that events with the appropriate orientation can safely be detected up to a radial distance of 5 km. Outside of this region, however, the rays reach

vertical turning points and precise source localization becomes difficult. For this reason in the following we, somewhat arbitrarily, limit the fiducial volume to 5 km radius. Since, in reality, signals from outside of this region will be detected albeit with unknown efficiency, our acceptance estimate will be a conservative one. In practice the requirement that the radiation “pancake” intercepts several hydrophones almost coplanar with the sea floor forces the direction of the accepted neutrinos to be close to the vertical.

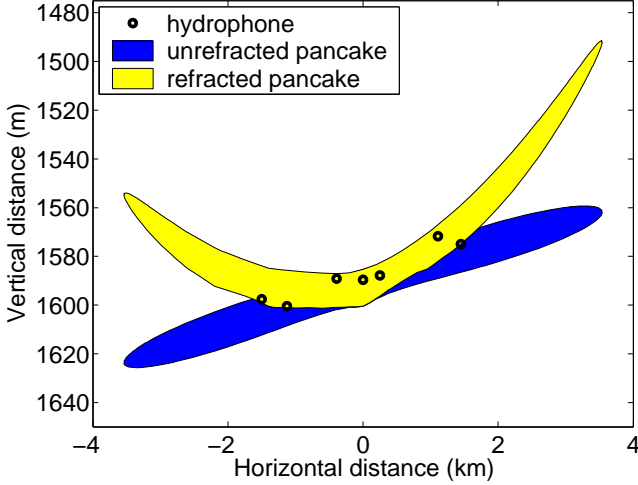


FIG. 14: The effect of refraction on the acoustic radiation envelope (pancake). A cross section of the acoustic radiation pattern from a  $10^{21}$  eV neutrino at  $0.5^\circ$  zenith is shown with and without refraction. Projections of the seven hydrophone locations onto the cross sections are shown for reference. Note that the detector is inclined to  $\sim 0.5^\circ$  zenith,  $7^\circ$  east of north, due to the slightly sloping sea floor.

The resolution in source position estimated from Monte Carlo worsens steadily with distance outside the array, but it does not exceed 500 m (vertical) and 200 m (horizontal) for radial distances smaller than 5 km. As shown in Figure 15, focusing effects due to refraction are small for sources in the neutrino fiducial volume and will be neglected. The position of detectable neutrino Monte Carlo events with energies of  $10^{14}$  GeV,  $10^{15}$  GeV, and  $10^{16}$  GeV are shown in a side (top) view in Figure 16 (Figure 17). The concentration of events slightly above the plane defined by the phones is consistent with the geometrical considerations above. The positions of the 79 acoustic events passing all analysis cuts in Run B are also shown as small squares. There is a clear separation between these events, mainly concentrated in the water column above the hydrophones, and the region where the neutrino events are expected to be. We hence conclude that the spatial distribution of observed events is incompatible with the one expected from neutrino interactions. The expected pancake shape of the acoustic emission profile from neutrinos is an essential assumption

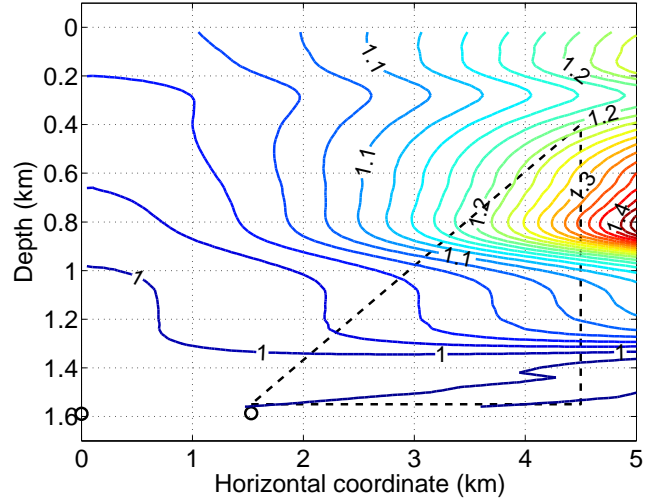


FIG. 15: Degree of acoustic flux focusing at the central hydrophone, for sources at various points as calculated from ray tracing. Contours of equal focusing are given. The dashed curve encloses the fiducial volume used for the neutrino analysis. Central and peripheral hydrophone locations are indicated by circles. Factors greater than one indicate focusing.

of this assertion.

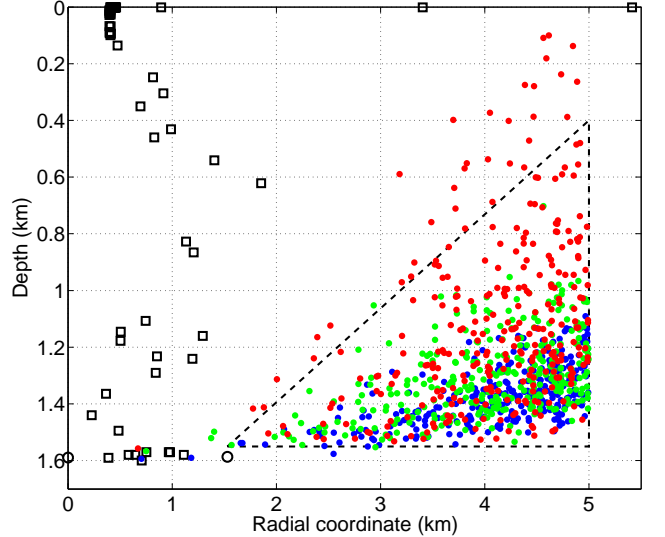


FIG. 16: Side view of reconstructed positions for the 79 coincidences surviving all cuts except for fiducial volume. The fiducial volume is bounded by the dashed triangle. Circles represent hydrophone positions and squares represent the 79 coincidences. 300 Monte Carlo events are also plotted, as colored dots, for each of three different energies,  $10^{14}$  GeV (blue),  $10^{15}$  GeV (green), and  $10^{16}$  GeV (red).

In order to express this result as an upper limit to the ultra high energy neutrino flux we define a fiducial volume given by the revolution of the dashed triangle around

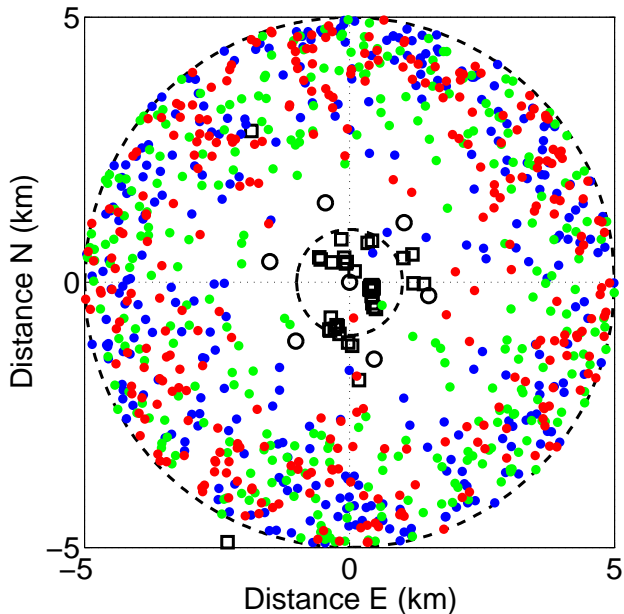


FIG. 17: Top view of the reconstructed positions for the 79 acoustic neutrino candidates surviving the selection cuts. The fiducial volume is bound by the two dashed circles. The small circles represent the positions of the hydrophones and the neutrino candidates are shown by the small squares. Monte Carlo events for three different energies are also shown with the same convention as in Figure 16.

the vertical axis. The fiducial region is chosen to be slightly above the ocean floor in order not to be affected by floor roughness. Ideally the fiducial volume choice would have been based entirely on the signal Monte Carlo events. However, given the novelty of the technique and the present emphasis on studying backgrounds, such a “blind” approach is impractical here. The separation between expected neutrino region and observed coincidences is nevertheless striking so that the definition of the fiducial volume is unambiguous. In fact, the main source of uncertainty in our analysis lies in the assumptions made about the phase response of the array. No 5-phone coincidences are present in SAUND Run B within the fiducial volume.

From the geometrical acceptance  $A(E, N_{\min})$  defined above a “neutrino exposure”  $X(E) = A(E)N_A\sigma(E)T(E)$  is computed. Here  $N_{\min}$  has been set to 5,  $N_A$  is the Avogadro number,  $\sigma(E)$  is the neutrino cross section and  $T(E)$  is the live time (also a function of the energy because of the dynamic threshold adjustment discussed in an earlier section).  $\sigma$  is estimated by extrapolating the power-law fit given for energies between  $10^{16}$  eV and  $10^{21}$  eV in [15]. Fits for neutrinos are used, the anti-neutrino ones being very similar. A 90% flux limit is then calculated [6] using Poisson’s statistics with the information that no events are observed. Such limit (multiplied

by  $E^2$ , as customary) is shown in Figure 18 along with the limits already available from FORTE [6], RICE [5] and GLUE [4], and with fluxes predicted by various theories.

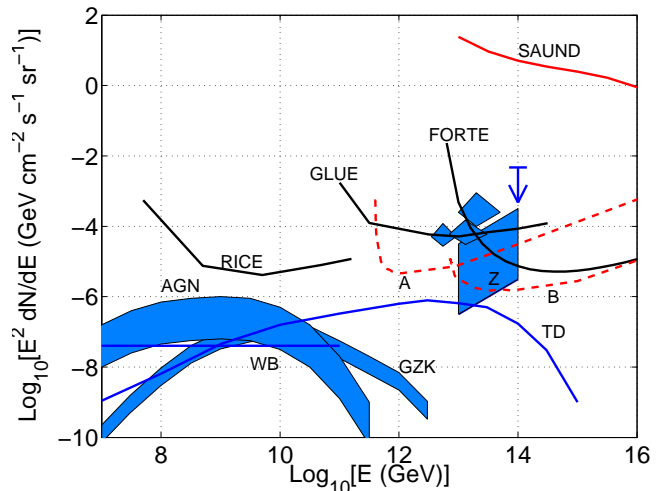


FIG. 18: Diffuse neutrino flux limit from SAUND and other experiments, and theoretical models of neutrino fluxes. The SAUND limit is shown in solid red. The hypothetical sensitivities of two different optimized acoustic arrays (A and B), described in the text, are shown as dashed red curves. Other experimental limits (FORTE, GLUE, and RICE) are shown in solid black. The blue curves and regions indicate various theoretical models: Z-bursts (one large trapezoid, three small quadrilaterals, and arrow), topological defects, active galactic nuclei, GZK neutrinos, and the Waxmann-Bahcall gamma-ray-burst limit.

## DISCUSSION

While the main motivation of this work has been to gain operational experience and investigate acoustic backgrounds for UHE neutrino detection, an effort was made to analyse the data in such a way as to obtain a flux measurement. Although the limit shown in Figure 18 is not competitive with the best ones, obtained with radio techniques, it represent the first UHE neutrino measurement performed with acoustic techniques. A wealth of information on noise conditions and the possible methods available to separate such noise from the neutrino signals has been obtained. Here we briefly analyze the characteristics of the SAUND array that turned out not to be optimal for UHE neutrino detection and we describe some of the properties that an optimized acoustic array should have.

The flatness of the acoustic radiation lobes from UHE showers is a crucial feature that allows noise rejection but also drastically limits the acceptance of SAUND. Refraction exacerbates the problem, by making regions

of sea invisible to the array and by curving the emission “pancake” into a shape that often has little overlap with a planar hydrophone array. The planar geometry of the SAUND array is also poorly optimized to provide good position resolution in the direction orthogonal to the plane. The vertical resolution is estimated to approach 400 m for sources below 1400 m depth while it is 10 m for sources close to the surface. The resolution in the horizontal plane, however, is better than 10 m in most of the volume. A hydrophone array on a 3D lattice would provide, at the same time, consistently better position resolution and substantially larger acceptance.

Although the long attenuation length of sound in water allows large (several hundred meters to several kilometers) horizontal spacing for an optimized neutrino detector, to overcome the flatness of the acoustic radiation an array with dense vertical spacing (10 m or lower) is necessary. The ideal array would be one of vertical strings with uniform sensitivity along their entire length. Such a detector element is not inconceivable could perhaps be realized with a tube of fluid with a sound speed different from the surrounding water, attached to hydrophones on each end. When an acoustic signal intercepts the tube, the difference in sound speeds leads to a signal propagating in both directions along the tube. The difference in arrival times at the two hydrophones could be used to localize the intersection point. Alternative schemes may involve interferometers built with an optical fiber running along the length of the string.

To explore the possible sensitivity of a detector using such strings, two hypothetical arrays were simulated with Monte Carlo neutrinos. Both are hexagonal lattices of 367 1.5 km-long strings. The first (“A”) has 500 m nearest-neighbor spacing and is bounded by a circle of radius  $R = 5$  km drawn about the central string. The second (“B”) has 5 km spacing and is bounded by an  $R = 50$  km circle. Both are taken to have a fiducial volume given by a cylinder of height 1.5 km and radius  $R + 5$  km. Circles of various radii representing acoustic radiation from neutrinos of various energies were generated throughout this fiducial volume, with zenith from 0 to  $\pi/2$ . The calculated sensitivity of these arrays, requiring 5 strings hit, is given in Figure 18. It is possible that more advanced triggering schemes, in which thresholds are lowered for a time window after a first sensor is hit, may allow for better sensitivity at lower energy.

Finally, the present work has clearly shown the importance of the calibration of the phase response of the acoustical array. In absence of such a calibration it is expected that the unknown phase properties of the readout will dominate the systematics of the measurement. An artificial source capable of providing acoustic signals similar to those from neutrinos with energies somewhere in the middle of the range considered here can be realized discharging a capacitor in a column of sea water of length similar to that of a UHE shower. The instantane-

ous heating of the water should closely simulate the heating produced by showers, releasing an acoustic wave with the right pancake geometry and phase/frequency structure.

## ACKNOWLEDGMENTS

We would like to thank the US Navy and, in particular, D. Belasco, J. Cecil, D. Deveau, and T. Kelly-Bissonnette, for hospitality and help at the AUTECH site. Many illuminating discussions with M. Buckingham and T. Berger (Scripps Institution of Oceanography) are gratefully acknowledged. We thank Y. Zhao (Stanford) for help with the data analysis and N. Kurahashi for a careful reading of the manuscript. One of us (JV) would like to thank M. Oreglia at the University of Chicago for hospitality during part of this work. This work was supported, in part, by NSF Grant PHY0354497 and by a Stanford University Terman fellowship.

- 
- \* Now at the University of California, Berkeley
  - † Now at the University of Hawaii, Manoa
  - [1] K. Greisen, Phys. Rev. Lett. 16 (1966) 748; G.T. Zatsepin and V.A. Kuzmin, JETP Lett. 4 (1966) 78.
  - [2] H. Takeda *et al.*, Astrophys. J. 522 (1999) 225.
  - [3] R.U. Abbasi *et al.*, astro-ph/0208243.
  - [4] P. Gorham *et al.*, astro-ph/0310232, to appear in Phys. Rev. Lett.
  - [5] I. Kravchenko *et al.* Astropart. Phys. 20 (2003) 195.
  - [6] N. Lehtinen *et al.* Phys. Rev. D 69 (2004) 013008.
  - [7] G.A. Askaryan, Sov. J. Atom. Energy 3 (1957) 921; G.A. Askaryan and B.A. Dolgoshein JETP Lett. 25 (1977) 213.
  - [8] J.G. Learned, Phys. Rev. D 19 (1979) 3293.
  - [9] L. Sulak *et al.*, Nucl. Inst. Meth. 161 (1979) 203.
  - [10] N.G. Lehtinen *et al.*, Astropart. Phys. 17 (2002) 279.
  - [11] <http://www.npt.nuwc.navy.mil/autec/>
  - [12] National Instruments Model PCI MIO 16E1.
  - [13] We note here that an erroneous value for the volume expansivity of seawater was used in [10]. A value of  $1.2 \times 10^{-3}$  was used instead of the correct value of  $0.15 \times 10^{-3}$ . This resulted in a simulated signal amplitude larger than the correct value by a factor of 8. This error is corrected in the present work.
  - [14] J. Kwiecinski *et al.*, Phys. Rev. D 59 (1999) 093002.
  - [15] R. Gandhi *et al.*, Astropart. Phys. 5 (1996) 81.
  - [16] L.D. Landau and I. Pomeranchuk, Dokl. Akad. Nauk USSR 92 (1953) 535; L.D. Landau and I. Pomeranchuk, Dokl. Akad. Nauk USSR 92 (1953) 735; A.B. Migdal, Phys. Rev. 103 (1956) 1811; A.B. Migdal, Sov. Phys. JETP 5 (1957) 527.
  - [17] J. Alvarez-Muniz and E. Zas, Phys. Lett. B 434 (1998) 396.
  - [18] R.V. Hogg and A.T. Craig, “Introduction to Mathematical Statistics”, 5<sup>th</sup> ed., Macmillan College Pub. Co., New York, 1995.

- [19] V.O. Knudsen, R.S. Alford and J.W. Emling, *J. Marine Res.* 7 (1948) 410.
- [20] For the most common household (“A19” sized) incandescence bulbs ( $\sim 6.7$  cm diameter); no signal was detected from miniaturized bulbs, possibly because no implosion occurs.
- [21] Magellan, Model 310.
- [22] G.J. Heard *et al.* in OCEANS '97, IEEE Conference Proceedings 2 (1997) 755.
- [23] A classical TDOA reference for silly particle astrophysicists.
- [24] W.A. Watkins and W.E. Schevill, “Four hydrophone arrays for acoustic three-dimensional location”, Woods Hole Oceanographic Institute Technical Report No. 71-60, 1971.
- [25] C.A. Boyles, “Acoustic waveguides : applications to oceanic science”, Wiley, New York, 1984.
- [26] D.F. Gaitan *et al.*, *J. Acoust. Soc. Am.* 91 (1992) 3166; J.B. Keller and I.I. Kolodner, *J. Appl. Phys.* 27 (1956) 1152; J.B. Keller and M. Miksis, *J. Acoust. Soc. Am.* 68 (1980) 628.